bioRxiv preprint doi: https://doi.org/10.1101/2020.01.05.895003; this version posted February 29, 2020. The copyright holder for this preprint (which was not certified by peer review) is the author/funder. This article is a US Government work. It is not subject to copyright under 17 USC 105 and is also made available for use under a CC0 license.

Dense cellular segmentation using 2D-3D neural network ensembles for electron microscopy

Matthew Guay[1,+,*], **Zeyad Emam**[1,2,+], **Adam Anderson**[1,2], **Maria Aronova**[1], **and Richard Leapman**[1]

[1]National Institute of Biomedical Imaging and Bioengineering, NIH, Bethesda, 20892, USA
[2]University of Maryland, College Park, 20740
[*]matthew.guay@nih.gov
[+]these authors contributed equally to this work

ABSTRACT

Modern biological electron microscopy produces nanoscale images from biological samples of unprecedented volume, and researchers now face the problem of making use of the data. Image segmentation has played a fundamental role in EM image analysis for decades, but challenges from biological EM have spurred interest and rapid advances in computer vision for automating the segmentation process. In this paper, we demonstrate dense cellular segmentation as a method for generating rich 3D models of tissues and their constituent cells and organelles from scanning electron microscopy images. We describe how to use ensembles of 2D-3D neural networks to compute dense cellular segmentations of cells and organelles inside two human platelet tissue samples. We conclude by discussing ongoing challenges for realizing practical dense cellular segmentation algorithms. The data and code used in this paper, as well as example notebooks, are available at `leapmanlab.github.io/dense-cell`.

Biomedical researchers use electron microscopy (EM) to image cells, organelles, and their constituents at the nanoscale. The serial block-face scanning electron microscope (SBF-SEM)[1] uses automated serial sectioning techniques to rapidly produce gigavoxel image volumes and beyond. This rapid growth in throughput challenges traditional image analytic workflows for EM, which rely on trained humans to identify salient image features. High-throughput EM offers to revolutionize systems biology by providing nanoscale structural detail across macroscopic tissue regions, but analyses of such datasets in their entirety will be infeasibly expensive and time-consuming until analytic bottlenecks are automated.

A fundamental component of common EM image anaylsis workflows is segmentation, which groups image voxels together into labeled regions that correspond to image content. For semantic segmentation, each voxel is assigned an object classification label, such as `cell` or `mitochondrion`. In this paper we introduce a **dense cellular segmentation** task, illustrated in Figure 1, which seeks to segment the entirety of an image volume with multiple, detailed class labels. Dense semantic segmentation is vital for systems biologists seeking to create semantically-rich 3D models of cells and subcellular structure interconnected within tissue environments.

Manually performing dense segmentation tasks for EM volumes is tedious and infeasible at scale for new high-throughput microscopes. However, automating dense segmentation for EM is challenging due to the image complexity of biological structures at the nanoscale. An image with little noise and high contrast between features may be accurately segmented with simple methods such as thresholding[2], while accurate segmentation of complicated images with multiscale features, noise, and textural content remains an open problem for many tasks of interest to biomedicine. Current state-of-the-art computational solutions use convolutional neural network architectures to solve problems on a per-task basis. The field of connectomics has spurred a number of advances in biomedical segmentation in its pursuit of accurate neural circuit tracing[?,3], but there are few solutions for other analysis problems facing systems biologists, and working with 3D data presents challenges for common compute hardware to properly exploit 3D spatial context during classification.

In this paper, we introduce a new 3D biomedical segmentation algorithm based on ensembles of neural networks

bioRxiv preprint doi: https://doi.org/10.1101/2020.01.05.895003; this version posted February 29, 2020. The copyright holder for this preprint (which was not certified by peer review) is the author/funder. This article is a US Government work. It is not subject to copyright under 17 USC 105 and is also made available for use under a CC0 license.

with separate 2D and 3D prediction modules, building off of existing work in volumetric image segmentation[4–6] to solve a dense segmentation task for a platelet SBF-SEM dataset. The resulting segmentation algorithms outperform existing 3D segmentation networks trained on our platelet segmentation task. We also highlight a challenge for validating segmentation network design choices - the wide distribution of trained architecture performance results due to random initialization - and offer a simple solution to make better-informed conclusions on segmentation network architecture design.

Prior Work

In recent years, deep convolutional neural networks (CNNs) became the *de facto* algorithms on most computer vision tasks[3,7,8]. The field of 2D segmentation of natural images has received enormous attention, with major companies releasing sophisticated trained models in the pursuit of solutions to vision problems of economic importance[9–12]. Work in biomedical image segmentation has been comparatively modest, with more work done in medical imaging such as radiology[13–15] than in microscopy, but important precedents do exist. A seminal contribution from this area was the U-Net[3], which spawned numerous encoder-decoder variants sporting architectural improvements[16–18]. The proliferation of volumetric data in biomedicine has also spurred developments in 3D segmentation[4,19–25], though the field lacks high-quality benchmark datasets for comparing different segmentation algorithms. For this paper, we adapted existing 2D DeeplabV3[10], 3D DeepVess[25], and 2D and 3D U-Net architectures to our segmentation task as a baseline for our new results.

Results

Dense cellular segmentation. When performed by humans, high-quality semantic segmentations of cells and organelles are the result of feedback between teams of scientific image annotators and subject matter experts, but this is a process that cannot easily scale to large volumes of data. Here, we demonstrate a segmentation algorithm that improves over baseline results, with quality approaching human image annotators and with similar performance on a common downstream biological image processing task. In addition to comparing our network output with the high-quality ground truth labels finalized through a time-consuming dialogue between research teams, we also compare it with the initial output of two in-lab scientific image annotators on an additional test region.

The datasets used in this study consist of 3D electron microscopy image volumes from two human patient platelet samples. From the two physical samples Patient1 and Patient2, this paper focuses on four datasets: *training data* ($50 \times 800 \times 800$ voxels), *eval data* ($24 \times 800 \times 800$ voxels), *test data* ($121 \times 609 \times 400$ voxels), and *annotator comparison data* ($110 \times 602 \times 509$ voxels). The training and eval data are subvolumes taken from Patient1. The test data and annotator comparison data are taken from Patient2. The training and evaluation ground truth labels covered the entirety of their respective images, while the test and annotator comparison labels each covered a single cell contained within their image volumes. The labeling schema divides image content into seven classes: `background`, `cell`, `mitochondrion`, `canalicular vessel`, `alpha granule`, `dense granule`, and `dense granule core`.

For the main experiment of this study, we compare baseline architectures, our new architecture, and ablations of the new architecture on a dense cellular segmentation task. We determine that our algorithm outperforms baselines, and that the differentiating features of our final best architecture are responsible for the performance differences. All networks are trained by supervised learning from manually-annotated ground truth labels. The results of this experiment are shown in Figure 3 and Table 1. Table 1 lists several networks and ensembles of networks along with their performance metrics: $\text{MIoU}^{(all)}$ refers to the mean IoU score across all classes, while $\text{MIoU}^{(org)}$ refers to the mean IoU score over the organelle classes only, not considering the background and cell body; *Eval* refers to the evaluation data consisting of a subset of Patient 1's data which is held-out during training; *Test* refers to the test data consisting of a single cell from patient 2. *We consider performance on the test data to be the best indicator of an algorithm's performance* as it shows its ability to generalize across different samples. Figure 3 compares visualizations of the best 2D and 3D segmentation algorithms with ground-truth labels and image data for the test and eval datasets. The results show that the best 3D algorithm improves considerably over the best 2D algorithm,

bioRxiv preprint doi: https://doi.org/10.1101/2020.01.05.895003; this version posted February 29, 2020. The copyright holder for this preprint (which was not certified by peer review) is the author/funder. This article is a US Government work. It is not subject to copyright under 17 USC 105 and is also made available for use under a CC0 license.

and that an ensemble of the top four 2D-3D+3x3x3 networks performs best. However, all algorithmic segmentations shown here still partially misclassify organelles, and label small organelle regions not identified by human labelers. Some of these may be actual organelles missed by humans, while others are spurious. Postprocessing the algorithmic results with small region removal fails to significantly affect Test MIoU$^{(org)}$ scores - tuning the region removal volume threshold to the test dataset produces a peak MIoU$^{(org)}$ of 0.4508. The multiscale nature of the correct image content frustrates such a simple cleanup strategy.

We also compare our best algorithm against the initial segmentations of scientific image annotators, Annotator 1 and Annotator 2. These are in-lab staff who are trained on annotation tasks but are not biological domain experts. These initial segmentations are currently the first step in producing high-quality dense cellular segmentations, and even before the correction process they are time-consuming to create. Results are displayed in Figure 5. Annotator 1, Annotator 2, and our algorithm each labeled the annotator comparison region from the Patient 2 platelet sample. We calculated MIoU$^{(org)}$ scores pairwise from the three segmentations: 0.571 for Annotator 1 vs. Annotator 2, 0.497 for Annotator 1 vs. Algorithm, and 0.483 for Annotator 2 vs. Algorithm. The confusion matrices in the bottom row of Figure 5 further break down results by organelle class. The statistics indicate that our algorithm disagrees more with either annotator than the annotators do with each other, but all label sources have inconsistent agreement across organelle types.

Beyond looking at the quality of the segmentation as an end, we are also interested in understanding how even imperfect segmentations may be useful for downstream analysis tasks. To this end, we computed organelle volume fractions for each organelle within the cell in the annotator comparison dataset. The cell volume fraction of an organelle is equal to the summed voxels of all organelles in a cell, divided by the cell's volume. To compute this quantity for each organelle, the number of voxels for each organelle label is divided by the number of voxels in the cell. An approximation was necessary for the algorithmic result. Since the algorithm does not distinguish between separate cells in contact with one another, a region for the cell was estimated as all labeled voxels within four voxels of the Annotator 1 cell mask. The results in the top right of Figure 5 show that the algorithm tended to underestimate volume fractions relative to the two annotators, but the difference between the algorithm and Annotator 1 is smaller than the difference between Annotator 1 and Annotator 2.

2D-3D networks. Convolutional neural networks used for semantic segmentation routinely have millions of parameters and dozens of layers arranged as a complicated hierarchy of interconnected computational modules, the result of dozens of choices in architecture design. When possible it is preferable to re-use an existing architecture, so we adapted popular biomedical and natural image segmentation architectures to our task. These presented obstacles however - naively converting 2D networks to 3D may present memory problems when trying to maintain a similar field of view, so large 2D natural image segmentation networks could not be adapted simply to our task. Existing popular fully-3D networks are smaller to reduce memory footprints, and may lack the capcity to learn challenging segmentation tasks. Inspired by existing work on combining 2D and 3D computations for volumetric data, both in deep learning[5,6] and more generally[26], we experimented with combinations of 2D and 3D neural modules to trade off between computational efficiency and spatial context. The highest-performing network architecture in this paper, 2D-3D+3x3x3, is a composition of a 2D U-net-style encoder-decoder and 3D convolutional spatial pyramid, with additional 3x3x3 convolutions at the beginning of convolution blocks in the encoder-decoder. All convolutions are zero-padded to preserve array shape throughout the network, allowing deep architectures to operate on data windows with small z-dimension. A detailed diagram of the network's architecture can be found in Figure 2.

Top-k ensembling. A common strategy for boosting the performance of a classification model is to form an ensemble prediction - averaging the predictions of multiple classifiers. For our segmentation networks, this means averaging the per-voxel probability distributions that each network predicts over possible class labels, and then forming a segmentation from the average. In this work, the ensembled networks are identical architectures trained from different random weight initializations. This ensembling approach, while simple, was obtained "for free" as we trained multiple initializations during model validation anyway, and the best result was a 7.0% improvement over using a single best network alone. When describing segmentation algorithms, we use Top-k to indicate an ensemble of the best k instances of an architecture.

Our Top-4 2D-3D+3x3x3 model performs best on the test data scoring 44.6% MIoU$^{(org)}$ while the next best ensemble

bioRxiv preprint doi: https://doi.org/10.1101/2020.01.05.895003; this version posted February 29, 2020. The copyright holder for this preprint (which was not certified by peer review) is the author/funder. This article is a US Government work. It is not subject to copyright under 17 USC 105 and is also made available for use under a CC0 license.

only achieves 42.1% $\text{MIoU}^{(org)}$. Our best model significantly improves segmentation results compared to all baseline networks. We also significantly outperform the best ensemble of 2D U-Nets, improving the test $\text{MIoU}^{(org)}$ by 20%. Our ablation analysis confirms our conjectures about the importance of 3D context input to the network, and the importance of 3x3x3 convolutions over 1x3x3 convolutions for generalization performance. The latter do not capture correlations along the z spatial dimension, likely contributing to their poorer performance. Ablation analysis also indicates that removing either the multi-loss training setup or the 3D spatial pyramid module from the 2D-3D+3x3x3 architecture carries significant performance penalties.

We have also tried using the DeepVess model from (Haft-Javaherian et al., 2019)[21] on our data. However, DeepVess performed poorly, and learned to assign a single class (background) to the entire output patch. We believe there may be two reasons behind DeepVess' poor performance: (1) Unlike U-Net and Deeplab networks, the DeepVess network is designed with very small input patches in mind; small patches do not contain enough context for the network to distinguish between objects. (2) DeepVess's last layer consists of a fully-connected operation with a single hidden layer containing 1024 neurons, therefore any attempt to input significantly larger patches would require increasing the number of neurons in the last layer, but fully-connected layers do not scale well and the network quickly outgrows GPU memory.

Initialization-dependent performance. In Figure 4 we experiment with various weight initialization random seeds to determine the robustness of various models to the weight initialization scheme. In order to determine whether one architecture choice is superior to another, the outputs of different trained networks are compared with each other. However, sources of randomness in the training process (initialization of trainable weights from a Xavier uniform distribution, and the random presentation order of training data elements) induce a distribution of final performance metric scores. These scores are random variables, and a single sample per architecture may be insufficient to determine which is better. By empirically approximating the distribution for each architecture, better inferences may be made about architecture design choices. For this figure, multiple instances of the same architecture (26 for 2D-3D and fully-3D nets, 500 for the U-Net) were trained under identical conditions, varying only random number generation seeds. The resulting distributions support the conclusions that 2D-3D networks outperform their 2D and fully-3D counterparts.

Discussion

In this work, we argued that dense semantic labeling of 3D EM images for biomedicine is an image analysis method with transformative potential for systems biology. We demonstrated that while challenges exist for both human and algorithmic labelers, automated methods are approaching the performance of trained humans, and may soon be integrated into annotation software for enhancing the productivty of humans segmenting large datasets. We introduced a new hybrid 2D-3D convolutional neural network architecture and demonstrated that it outperforms baseline networks on our platelet segmentation task, and that the novel architecture features are responsible for performance improvements. We do this by training multiple network instances per architecture and comparing the resulting trained network performance distributions, in order to account for variation introduced by randomness in the training procedure.

We conclude that the procedure of training neural network ensembles on a manually annotated portion of a large SBF-SEM dataset is becoming viable for accelerating the segmentation of biological SBF-SEM datasets, but that challenges remain for creating algorithms that are robust to the many types of variation present across research applications. SBF-SEM analysis problems are a fertile early ground for computer vision research, as their large size makes the entire train-test-deploy cycle of supervised learning viable for accelerating data analysis of even individual samples. We suggest future developments to integrate predictive tools and manual annotation, as well as a broad program of additional research to create more accurate and more robust biological volumetric segmentation algorithms. In this paper, we have highlighted the dense semantic segmentation task and suggested a way forward for developing better algorithms to enable this method to be useful in practice. Our aim is to spur the research and development of techniques to make large-scale EM imaging more useful to systems biology as a field.

bioRxiv preprint doi: https://doi.org/10.1101/2020.01.05.895003; this version posted February 29, 2020. The copyright holder for this preprint (which was not certified by peer review) is the author/funder. This article is a US Government work. It is not subject to copyright under 17 USC 105 and is also made available for use under a CC0 license.

References

1. Denk, W. & Horstmann, H. Serial Block-Face Scanning Electron Microscopy to Reconstruct Three-Dimensional Tissue Nanostructure. *PLoS Biol.* **2**, DOI: 10.1371/journal.pbio.0020329 (2004).
2. Kurita, T., Otsu, N. & Abdelmalek, N. Maximum likelihood thresholding based on population mixture models. *Pattern recognition* **25**, 1231–1240 (1992).
3. Ronneberger, O., Fischer, P. & Brox, T. U-Net: Convolutional Networks for Biomedical Image Segmentation. In *LNCS*, vol. 9351, 234–241, DOI: 10.1007/978-3-319-24574-4_28 (2015).
4. Lee, K., Zlateski, A., Ashwin, V. & Seung, H. S. Recursive Training of 2d-3d Convolutional Networks for Neuronal Boundary Prediction. In Cortes, C., Lawrence, N. D., Lee, D. D., Sugiyama, M. & Garnett, R. (eds.) *Advances in Neural Information Processing Systems 28*, 3573–3581 (Curran Associates, Inc., 2015).
5. Chen, J., Yang, L., Zhang, Y., Alber, M. & Chen, D. Z. Combining fully convolutional and recurrent neural networks for 3d biomedical image segmentation. In *Advances in neural information processing systems*, 3036–3044 (2016).
6. Patravali, J., Jain, S. & Chilamkurthy, S. 2d-3d fully convolutional neural networks for cardiac mr segmentation. In *International Workshop on Statistical Atlases and Computational Models of the Heart*, 130–139 (Springer, 2017).
7. Krizhevsky, A., Sutskever, I. & Hinton, G. E. ImageNet Classification with Deep Convolutional Neural Networks. In Pereira, F., Burges, C. J. C., Bottou, L. & Weinberger, K. Q. (eds.) *Advances in Neural Information Processing Systems 25*, 1097–1105 (Curran Associates, Inc., 2012).
8. He, K., Zhang, X., Ren, S. & Sun, J. Deep Residual Learning for Image Recognition. In *2016 IEEE Conference on Computer Vision and Pattern Recognition (CVPR)*, 770–778, DOI: 10.1109/CVPR.2016.90 (2016). ISSN: 1063-6919.
9. Kirillov, A., He, K., Girshick, R., Rother, C. & Dollár, P. Panoptic segmentation. In *Proceedings of the IEEE Conference on Computer Vision and Pattern Recognition*, 9404–9413 (2019).
10. Chen, L.-C., Papandreou, G., Schroff, F. & Adam, H. Rethinking atrous convolution for semantic image segmentation. *arXiv preprint arXiv:1706.05587* (2017).
11. Chen, L.-C., Papandreou, G., Kokkinos, I., Murphy, K. & Yuille, A. L. Deeplab: Semantic image segmentation with deep convolutional nets, atrous convolution, and fully connected crfs. *IEEE transactions on pattern analysis machine intelligence* **40**, 834–848 (2017).
12. Redmon, J., Divvala, S., Girshick, R. & Farhadi, A. You only look once: Unified, real-time object detection. In *Proceedings of the IEEE conference on computer vision and pattern recognition*, 779–788 (2016).
13. Greenspan, H., Van Ginneken, B. & Summers, R. M. Deep learning in medical imaging: Overview and future promise of an exciting new technique. *IEEE Transactions on Med. Imaging* **35**, 1153–1159 (2016).
14. Hosny, A., Parmar, C., Quackenbush, J., Schwartz, L. H. & Aerts, H. J. Artificial intelligence in radiology. *Nat. Rev. Cancer* **18**, 500–510 (2018).
15. Sahiner, B. *et al.* Deep learning in medical imaging and radiation therapy. *Med. physics* **46**, e1–e36 (2019).
16. Milletari, F., Navab, N. & Ahmadi, S.-A. V-net: Fully convolutional neural networks for volumetric medical image segmentation. In *2016 Fourth International Conference on 3D Vision (3DV)*, 565–571 (IEEE, 2016).
17. Long, J., Shelhamer, E. & Darrell, T. Fully convolutional networks for semantic segmentation. In *Proceedings of the IEEE conference on computer vision and pattern recognition*, 3431–3440 (2015).
18. Badrinarayanan, V., Kendall, A. & Cipolla, R. Segnet: A deep convolutional encoder-decoder architecture for image segmentation. *IEEE transactions on pattern analysis machine intelligence* **39**, 2481–2495 (2017).

bioRxiv preprint doi: https://doi.org/10.1101/2020.01.05.895003; this version posted February 29, 2020. The copyright holder for this preprint (which was not certified by peer review) is the author/funder. This article is a US Government work. It is not subject to copyright under 17 USC 105 and is also made available for use under a CC0 license.

19. Chen, H., Dou, Q., Yu, L., Qin, J. & Heng, P.-A. VoxResNet: Deep voxelwise residual networks for brain segmentation from 3d MR images. *NeuroImage* **170**, 446–455, DOI: 10.1016/j.neuroimage.2017.04.041 (2018).

20. Chen, S., Ma, K. & Zheng, Y. Med3d: Transfer Learning for 3d Medical Image Analysis. *arXiv:1904.00625 [cs]* (2019). ArXiv: 1904.00625.

21. Haft-Javaherian, M. *et al.* Deep convolutional neural networks for segmenting 3d in vivo multiphoton images of vasculature in Alzheimer disease mouse models. *PLoS ONE* **14**, DOI: 10.1371/journal.pone.0213539 (2019).

22. Roth, H. R. *et al.* An application of cascaded 3d fully convolutional networks for medical image segmentation. *Comput. Med. Imaging Graph.* **66**, 90–99, DOI: 10.1016/j.compmedimag.2018.03.001 (2018).

23. Wang, G. *et al.* DeepIGeoS: A Deep Interactive Geodesic Framework for Medical Image Segmentation. *IEEE Transactions on Pattern Analysis Mach. Intell.* **41**, 1559–1572, DOI: 10.1109/TPAMI.2018.2840695 (2019). ArXiv: 1707.00652.

24. Zhu, Z., Xia, Y., Shen, W., Fishman, E. & Yuille, A. A 3d Coarse-to-Fine Framework for Volumetric Medical Image Segmentation. In *2018 International Conference on 3D Vision (3DV)*, 682–690, DOI: 10.1109/3DV.2018.00083 (2018). ISSN: 2378-3826.

25. Fu, H., Xu, Y., Lin, S., Wong, D. W. K. & Liu, J. Deepvessel: Retinal vessel segmentation via deep learning and conditional random field. In *International conference on medical image computing and computer-assisted intervention*, 132–139 (Springer, 2016).

26. Zhu, Y., Williams, S. & Zwiggelaar, R. A hybrid asm approach for sparse volumetric data segmentation. *Pattern recognition image analysis* **17**, 252–258 (2007).

27. Stalling, D., Westerhoff, M., Hege, H.-C. *et al.* Amira: A highly interactive system for visual data analysis. *The visualization handbook* **38**, 749–67 (2005).

28. Krogh, A. & Vedelsby, J. Neural network ensembles, cross validation, and active learning. In *Advances in neural information processing systems*, 231–238 (1995).

29. Guay, M., Emam, Z., Anderson, A. & Leapman, R. Designing deep neural networks to automate segmentation for serial block-face electron microscopy. In *2018 IEEE 15th International Symposium on Biomedical Imaging (ISBI 2018)*, 405–408 (IEEE, 2018).

30. Çiçek, Ö., Abdulkadir, A., Lienkamp, S. S., Brox, T. & Ronneberger, O. 3d u-net: learning dense volumetric segmentation from sparse annotation. In *International conference on medical image computing and computer-assisted intervention*, 424–432 (Springer, 2016).

Methods

SBF-SEM image volumes were obtained from identically-prepared platelet samples from two humans. Lab members manually segmented portions of each volume into seven classes to analyze the structure of the platelets. The labels were used for the supervised training of candidate network architectures, as well as baseline comparisons. We trained multiple instances of candidate architectures, each with different random initializations. The best-performing instances were ensembled together to produce the final segmentation algorithms used in this paper.

Data collection

This study used datasets prepared from two human platelet samples as part of a collaborative effort between the National Institute of Biomedical Imaging and Bioengineering (NIBIB), NIH and the University of Arkansas for Medical Sciences. The platelet samples were imaged using a Zeiss 3View SBF-SEM. The Patient 1 dataset is a $250 \times 2000 \times 2000$ voxel image with a lateral resolution of 10 nm and an axial resolution of 50 nm, from a sample volume with dimensions $12.5 \times 20 \times 20 \mu m^3$. The Patient 2 dataset is a $239 \times 2000 \times 2000$ voxel image produced by the same imaging protocol, with the same resolution and coming from a sample volume with the same dimensions.

bioRxiv preprint doi: https://doi.org/10.1101/2020.01.05.895003; this version posted February 29, 2020. The copyright holder for this preprint (which was not certified by peer review) is the author/funder. This article is a US Government work. It is not subject to copyright under 17 USC 105 and is also made available for use under a CC0 license.

We assembled labeled datasets from manually-segmented regions of the platelet datasets. Lab members created initial manual segmentations using Amira[27]. For the training, evaluation, and test dataset, segmentations were reviewed by subject experts and corrected. The training image was a $50 \times 800 \times 800$ subvolume of the Patient 1 dataset spanning the region $81 \leq z \leq 130$, $1073 \leq y \leq 1872$, $620 \leq x \leq 1419$ in 0-indexed notation. The evaluation image was a $24 \times 800 \times 800$ subvolume of the Patient 1 dataset spanning the region $100 \leq z \leq 123$, $200 \leq y \leq 999$, $620 \leq x \leq 1419$. The test image was a $121 \times 609 \times 400$ subvolume of the Patient 2 dataset spanning the region $0 \leq z \leq 120$, $460 \leq y \leq 1068$, $308 \leq x \leq 707$. The annotator comparison image was a $110 \times 602 \times 509$ subvolume of the Patient 2 dataset spanning the region $116 \leq z \leq 225$, $638 \leq y \leq 1239$, $966 \leq x \leq 1474$. The training and evaluation labels covered the entirety of their respective images, while the test and annotator comparison labels covered a single cell contained within their image volumes. The labeling schema divides image content into seven classes: `background`, `cell`, `mitochondrion`, `canalicular vessel`, `alpha granule`, `dense granule`, and `dense granule core`.

Neural architectures and ensembling

The Patient 1 and Patient 2 datasets were binned by 2 in x and y, and aligned. For each of the training, evaluation, and testing procedures, the respective image subvolumes were normalized to have mean 0 and standard deviation 1 before further processing.

The highest-performing network architecture in this paper, 2D-3D+3x3x3, is a composition of a 2D U-net-style encoder-decoder and 3D convolutional spatial pyramid, with additional 3x3x3 convolutions at the beginning of convolution blocks in the encoder-decoder. All convolutions are zero-padded to preserve array shape throughout the network, allowing deep architectures to operate on data windows with small z-dimension. A ReLU activation follows each convolution. All convolution and transposed convolutions use bias terms. The architecture is fully specified as a diagram in Figure 2. Additionally, several baseline comparison networks and three 2D-3D+3x3x3 ablation networks were also tested in this paper and are described in the Validation and Performance Metrics section.

To build a 2D-3D network, one can adapt a 2D U-net-style encoder-decoder module to work on 3D data by recasting 2D 3x3 convolutions as 1x3x3 convolutions, and 2D 2x2 max-pooling and transposed convolution layers as 1x2x2 equivalents. In this way, a 3D input volume can be processed as a sequence of independent 2D regions in a single computation graph, and the 2D and 3D modules can be jointly trained end-to-end. Intermediate 2D class predictions $\hat{x}_{2D}$ are formed from the 2D module output, and the 2D output and class predictions are concatenated along the feature axis to form an input to a 3D spatial pyramid module. The 3D module applies a 1x2x2 max pool to its input to form a two-level spatial pyramid with scales 0 (input) and 1 (pooled). The pyramid elements separately pass through convolution blocks, and the scale 1 block output is upsampled and added to the scale 0 block output with a residual connection to form the module output. 3D class predictions $\hat{x}_{3D}$ are formed from the 3D module output, and the final segmentation output $\hat{\ell}$ of the algorithm is a voxelwise argmax of the 3D class predictions. To build a 2D-3D+3x3x3 network, we inserted 3x3x3 convolution layers at the beginning of the first two convolution blocks in the 2D encoder and the last two convolution blocks in the 2D decoder.

Given a collection of networks' 3D class predictions, one can form an ensemble prediction by computing a voxelwise average of the predictions and computing a segmentation from that. Ensembling high-quality but non-identical predictions can produce better predictions[28], and there is reason to think that more sophisticated ensembles could be constructed from collections of diverse neural architectures[29], but in this paper we use a simple source of differing predictions to boost performance: ensembles of identical architectures trained from different random initializations. The sources of randomness in the training procedure are examined more thoroughly in the Validation and Performance Metrics section, but in our experiments this variation produced a small number of high-performing network instances per architecture with partially-uncorrelated errors.

Network training

Assume a network predicting classes $C = \{0, \ldots, 6\}$ for each voxel in a shape-(o_z, o_x, o_y) data window Ω containing $N = o_z o_x o_y$ voxels $\{v_i\}_{i=1}^{N}$. The ground-truth segmentation of this region is a shape-(o_z, o_x, o_y) array ℓ such that $\ell(v) \in C$ is the ground-truth label for voxel v. A network output prediction is a shape-$(7, o_z, o_x, o_y)$ array $\hat{x}$ such

bioRxiv preprint doi: https://doi.org/10.1101/2020.01.05.895003; this version posted February 29, 2020. The copyright holder for this preprint (which was not certified by peer review) is the author/funder. This article is a US Government work. It is not subject to copyright under 17 USC 105 and is also made available for use under a CC0 license.

that $x_v \triangleq \hat{x}(:,v)$ is a probability distribution over possible class labels for voxel v. The corresponding segmentation $\hat{\ell}$ is the per-voxel $\arg\max$ of $\hat{x}$. Inversely, from ℓ one may construct a shape-$(7, o_z, o_x, o_y)$ per-voxel probability distribution x such that $x_v(i) = 1$ if $i = \ell(v)$ and 0 if not, which is useful during training.

We trained our networks as a series of experiments, with each experiment training and evaluating 1 or more instances of a fixed network architecture. Instances within an experiment varied only in the random number generator (RNG) seed used to control trainable variable initialization and training data presentation order. In addition to the main 2D-3D+3x3x3 architecture, there were three ablation experiments - No 3x3x3 Convs, No Multi-Loss, No 3D Pyramid - and five baseline experiments - Original U-Net, 3D U-Net Thin, 3D U-Net Thick, Deeplab + DRN, and Deeplab + ResNet101. Instances were trained and ranked by evaluation dataset MIoU. Experiments tracked evaluation MIoU for each instance at each evaluation point throughout training, and saved the final weight checkpoint as well as the checkpoint with highest eval MIoU. In this work we report eval MIoU checkpoints for each instance. The 2D-3D+3x3x3 experiment and its ablations trained 26 instances for 40 epochs with minibatch size 1 (33k steps). The Original U-Net experiment trained 500 instances for 100 epochs with minibatch size 1 (180k steps). The 3D U-Net Thin experiment trained 26 instances for 100 epochs with minibatch size 1 (29k steps), and the 3D U-Net Thick experiment trained 26 instances for 100 epochs with minibatch size 1 (30k steps). The Deeplab + DRN and Deeplab + ResNet101 experiments trained 1 instance each for 200 epochs with minibatch size 4 (360k steps). Due to poor performance and slow training times of the Deeplab models, we deemed it unnecessary to train further instances. Networks were trained on NVIDIA GTX 1080 and NVIDIA Tesla P100 GPUs.

This subsection details the training of the 2D-3D+3x3x3 network. Baseline and ablation networks were trained identically except as noted in Validation and Performance Metrics. All trainable variables were initialized from Xavier uniform distributions. Each instance was trained for 40 epochs on shape-$(5, 300, 300)$ windows extracted from the training volume, and output a shape-$(7, 5, 296, 296)$ class prediction array. The number of windows in each epoch was determined by a window spacing parameter which determined the distance along each axis between the top-back-left corners of each window, here $(2, 100, 100)$, resulting in 828 windows per epoch. An early stopping criterion halted the training of any network that failed to reach a mean intersection-over-union (MIoU) of 0.3 after 10 epochs.

Networks were trained using a regularized, weighted sum of cross-entropy functions. The network has a set Θ trainable variables divided into four subsets: Θ_{2D} for variables in the 2D encoder-decoder module, Θ_{3D} for variables in the 3D spatial pyramid module, the single 1x1x1 convolution variable $\{\theta_{2DP}\}$ which produces intermediate 2D class predictions $\hat{x}_{2D}$ from the encoder-decoder's 64 output features, and the single 1x1x1 convolution variable $\{\theta_{3DP}\}$ which produces the final 3D class predictions $\hat{x}_{3D}$ from the spatial pyramid's 64 output features. Predictions are compared against ground-truth labels as

$$\begin{aligned} L(x, \hat{x}_{3D}, \hat{x}_{2D}; \Theta) = & \frac{1}{N} \sum_{i=1}^{N} \left[\mathcal{W} \otimes \mathcal{H}(x, \hat{x}_{3D})\right]_i + \frac{c_{2D}}{N} \sum_{i=1}^{N} \left[\mathcal{W} \otimes \mathcal{H}(x, \hat{x}_{2D})\right] \\ & + \lambda_{2D} \sum_{\theta \in \Theta_{2D}} \|\theta\|_2^2 + \lambda_{3D} \sum_{\theta \in \Theta_{3D}} \|\theta\|_2^2 + \lambda_P \left(\|\theta_{2DP}\|_2^2 + \|\theta_{3DP}\|_2^2\right), \end{aligned} \tag{1}$$

where $\lambda_{2D} = 1 \times 10^{-4.7}$ and $\lambda_{3D} = 1 \times 10^{-5}$ are L^2 regularization hyperparameters for the variables in Θ_{2D} and Θ_{3D}, $\lambda_P = 1 \times 10^{-9}$ is an L^2 regularization hyperparameter for the predictor variables θ_{2DP} and θ_{3DP}, and $c_{2D} = 0.33$ is a constant that weights the importance of the intermediate 2D class predictions in the loss function. $\mathcal{H}(x, \hat{x})$ is the voxelwise cross-entropy function, i.e.,

$$\mathcal{H}(x, \hat{x})_v \triangleq H(x_v, \hat{x}_v) \triangleq -\sum_{j=1}^{7} x_v(j) \log\left[\hat{x}_v(j)\right] = -x_v(\ell_v) \log\left[\hat{x}_v(\ell_v)\right].$$

$\mathcal{W}$ is a shape-$(5, 296, 296)$ array of weights; its Kronecker product with $\mathcal{H}$ produces a relative weighting of the cross-entropy error per voxel. This weighting strategy is based generally on the approach in (Ronneberger et al., 2015)[3]:

$$\mathcal{W} = w + \mathcal{W}_{cb} + \mathcal{W}_{ep}.$$

bioRxiv preprint doi: https://doi.org/10.1101/2020.01.05.895003; this version posted February 29, 2020. The copyright holder for this preprint (which was not certified by peer review) is the author/funder. This article is a US Government work. It is not subject to copyright under 17 USC 105 and is also made available for use under a CC0 license.

The initial $w = 0.01$ is a constant that sets a floor for the minimum weight value, W_{cb} is a class-balancing term such that $W_{cb,i} \propto 1/N_i$, where N_i is the number of occurences in the training data of ℓ_i. W_{ep} is an edge-preserving term that upweights voxels near boundaries between image objects and within small 2D cross-sections. In (Ronneberger et al., 2015) this is computed using morphological operations. We used a sum of scaled, thresholded diffusion operations to approximate this strategy in a manner that requires no morphology information. The weight file used in this paper is available with the rest of the platelet dataset at `leapmanlab.github.io/dense-cell`.

We employed data augmentation to partially compensate for the limited available training data. Augmentations were random reflections along each axis, random shifts in brightness ($\pm 12\%$) and contrast ($\pm 20\%$), and elastic deformation as in (Ronneberger et al., 2015). For elastic deformation, each 800x800 $x-y$ plane in the shape-$(50,800,800)$ training data and label arrays was displaced according to a shape-$(800,800,2)$ array of 2D random pixel displacement vectors, generated by bilinearly upsampling a shape-$(20,20,2)$ array of iid Gaussian random variables with mean 20 and standard deviation 0.6. During each epoch of training, a single displacement map was created and applied to the entire training volume before creating the epoch's batch of input and output windows. Training used the ADAM optimizer with learning rate 1×10^{-3}, $\beta_1 = 1 - 1 \times 10^{-1.5}$, $\beta_2 = 1 - 1 \times 10^{-2.1}$, and $\varepsilon = 1 \times 10^{-7}$. Training also used learning rate decay with an exponential decay rate of 0.75 every $1 \times 10^{3.4}$ training iterations.

Validation and performance metrics

The performance metric used in this work is mean intersection-over-union (MIoU) between ground-truth image segmentation ℓ's 7 labeled sets $\{L_j = v \in \Omega \,|\, \ell(v) = j\}_{j \in C}$ and predicted segmentation's $\hat{\ell}$ labeled sets $\{\hat{L}_j = v \in \Omega \,|\, \hat{\ell}(v) = j\}_{j \in C}$. Given two sets A and B,

$$\mathrm{IoU}(A,B) = \frac{|A \cap B|}{|A \cup B|}.$$

Then for segmentations ℓ and $\hat{\ell}$ with their corresponding labeled sets,

$$\mathrm{MIoU}(\ell,\hat{\ell}) = \frac{1}{7} \sum_{j \in C} \mathrm{IoU}(L_j, \hat{L}_j).$$

More generally, for a subset of labels $D \subseteq C$, one can compute the MIoU over D, or $\mathrm{MIoU}^{(D)}$, as

$$\mathrm{MIoU}^{(D)}(\ell,\hat{\ell}) = \frac{1}{|D|} \sum_{j \in D} \mathrm{IoU}(L_j, \hat{L}_j).$$

Here we are concerned with MIoU's over two sets of labels: $\mathrm{MIoU}^{(all)}$ over the set of all 7 class labels, and $\mathrm{MIoU}^{(org)}$ over the set of 5 organelle labels 2-7. Our network validation metrics were $\mathrm{MIoU}^{(all)}$ and $\mathrm{MIoU}^{(org)}$ on the evaluation dataset, and $\mathrm{MIoU}^{(org)}$ on the test dataset. Test data uses $\mathrm{MIoU}^{(org)}$ because the labeled region is a single cell among several unlabeled ones, and restricting validation to the labeled region invalidates MIoU stats for the background and cell classes (0 and 1). We include eval $\mathrm{MIoU}^{(org)}$ to quantify how performance drops between a region taken from the physical sample used to generate the training data, and a new physical sample of the same tissue system.

Using this procedure, the performance of the 2D-3D+3x3x3 network was compared against three ablations and five baseline networks. The three ablations each tested one of three features that distinguish the 2D-3D+3x3x3 network in this paper from similar baselines. The first, 2D+3x3x3 No 3x3x3 Convs, replaces the 3x3x3 convolutions in the net's encoder-decoder module with 1x3x3 convolutions that are otherwise identical. With this ablation, the network's encoder-decoder loses any fully-3D layers. The second, 2D+3x3x3 No Multi-Loss, modifies the loss function in Equation (1) by removing the term involving $\hat{x}_{2D}$ but otherwise leaving the architecture and training procedure unchanged. This ablation tests whether it is important to have auxiliary accuracy loss terms during training. The third ablation, 2D-3D+3x3x3 No 3D Pyramid, removes the 3D spatial pyramid module and 3D class predictor module from the network architecture, so that $\hat{x}_{2D}$ is the network's output. Correspondingly, the loss term involving $\hat{x}_{3D}$ is removed from Equation (1).

bioRxiv preprint doi: https://doi.org/10.1101/2020.01.05.895003; this version posted February 29, 2020. The copyright holder for this preprint (which was not certified by peer review) is the author/funder. This article is a US Government work. It is not subject to copyright under 17 USC 105 and is also made available for use under a CC0 license.

We implemented five baseline networks by adapting common models in the literature to our platelet segmentation problem. Three of these were 2D - The original U-Net[3] as well as two Deeplab variants[10,11] using a deep residual network (DRN) backbone and a ResNet101 backbone[8], minimally modified to output 7 class predictions. The original U-Net used $(572, 572)$ input windows and $(388, 388)$ output windows, while the Deeplab variants used $(572, 572)$ input and output windows. The two 3D networks were fully-3D U-Net variants adapted on the 3D U-Net in (Çiçek et al., 2016)[30] - 3D U-Net Thin and 3D U-Net Thick. The variants used same-padding, had three convolutions per convolution block, and two pooling operations in the encoder for convolution blocks at three spatial scales. The 3D U-Net Thin network used $(5, 300, 300)$ input windows and $(5, 296, 296)$ output windows, and pooling and upsampling operations did not affect the z spatial axis. The 3D U-Net Thick network used $(16, 180, 180)$ input windows and $(16, 180, 180)$ output windows, and pooled and upsampled along all three spatial axes.
To determine whether one architecture is superior to another, trained instances are compared with each other. However, sources of randomness in the training process induce a distribution of final performance metric scores across trained instances of an architecture, so that a single sample per architecture may be insufficient to determine which is better. While expensive, a collection of instances can be trained and evaluated to empirically approximate the performance distribution for each architecture. In this way, better inferences may be made about architecture design choices. Figure 4 shows the empirical performance distributions for the 26 trials of the 2D-3D+3x3x3 architecture and its three ablations, as well as the 26 trials of the 3D U-Net and 500 trials of the 2D Original U-Net. A final point of comparison was drawn between the top algorithm's performance and the initial work of in-lab scientific image annotators, Annotator 1 and Annotator 2. The three sources each labeled the annotator comparison region from the Patient 2 platelet sample. Pairwise $\text{MIoU}^{(org)}$ scores and organelle confusion matrices were calculated to compare the level of disagreement between two human labelings and between humans and the algorithm. We also computed organelle volume fractions for each segmentation to compare performance in segmentation applications to downstream analysis tasks. The cell volume fraction of an organelle is equal to the summed voxels of all organelles in a cell, divided by the cell's volume. To compute this quantity for each organelle, the number of voxels for each organelle label is divided by the number of voxels in the cell. For the algorithmic result, since the semantic segmentation map does not distinguish between separate cells in the field of view, a mask for the single annotator comparison dataset cell was approximated as all non-background-labeled voxels in a small region around the Annotator 1 cell mask.

Reproducibility

All data used in this experiment, as well as examples showing how to download and train neural networks used in this paper on the platelet segmentation task, can be found at `leapmanlab.github.io/dense-cell`.

bioRxiv preprint doi: https://doi.org/10.1101/2020.01.05.895003; this version posted February 29, 2020. The copyright holder for this preprint (which was not certified by peer review) is the author/funder. This article is a US Government work. It is not subject to copyright under 17 USC 105 and is also made available for use under a CC0 license.

List of figures

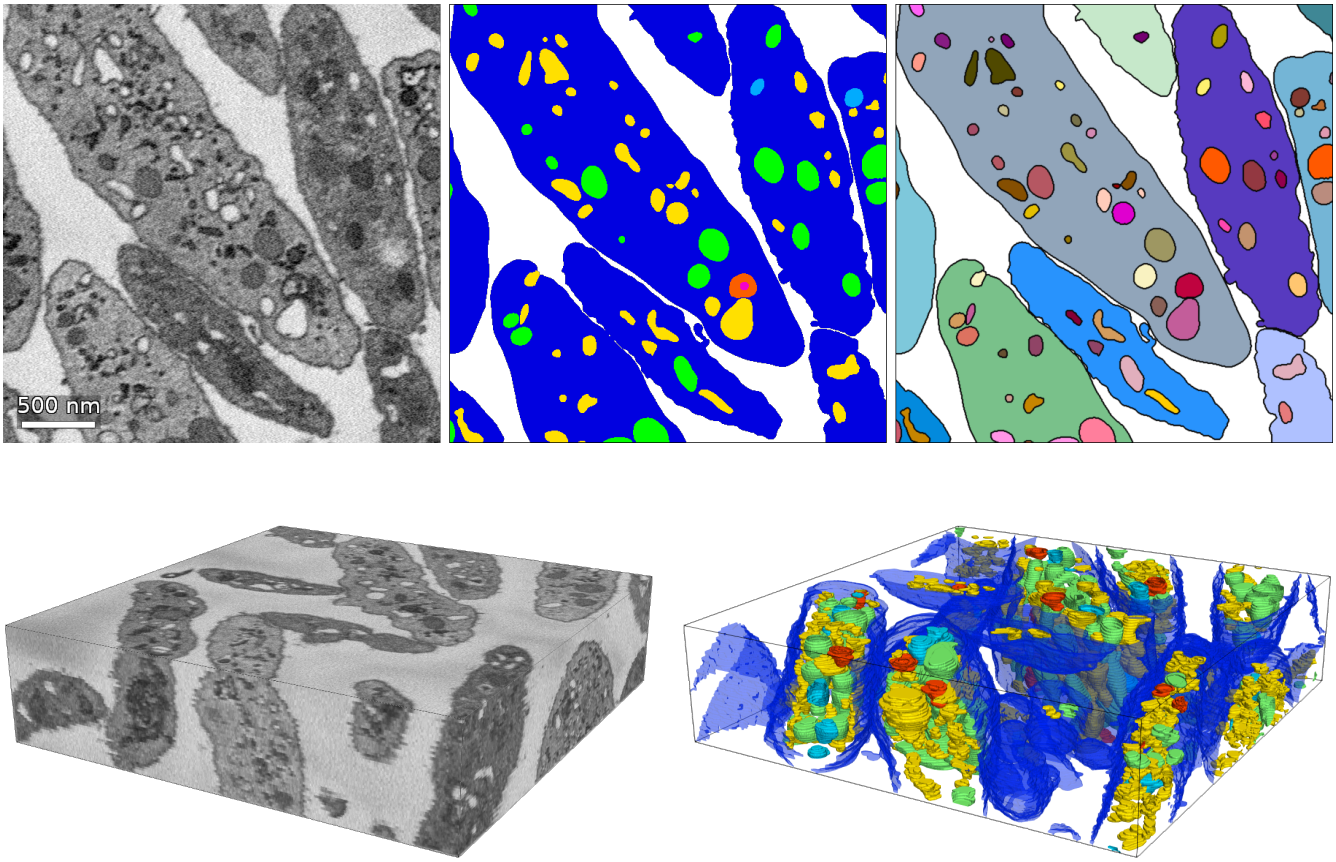

Figure 1. Overview of SBF-SEM imaging and dense cellular segmentation. (**Top**) Lateral (*x*-*y*) view of the platelet training dataset, its ground-truth segmentation into 7 semantic classes, and a digital cell model built from the semantic segmentation. (**Bottom**) 3D views of the training dataset and its ground-truth segmentation.

bioRxiv preprint doi: https://doi.org/10.1101/2020.01.05.895003; this version posted February 29, 2020. The copyright holder for this preprint (which was not certified by peer review) is the author/funder. This article is a US Government work. It is not subject to copyright under 17 USC 105 and is also made available for use under a CC0 license.

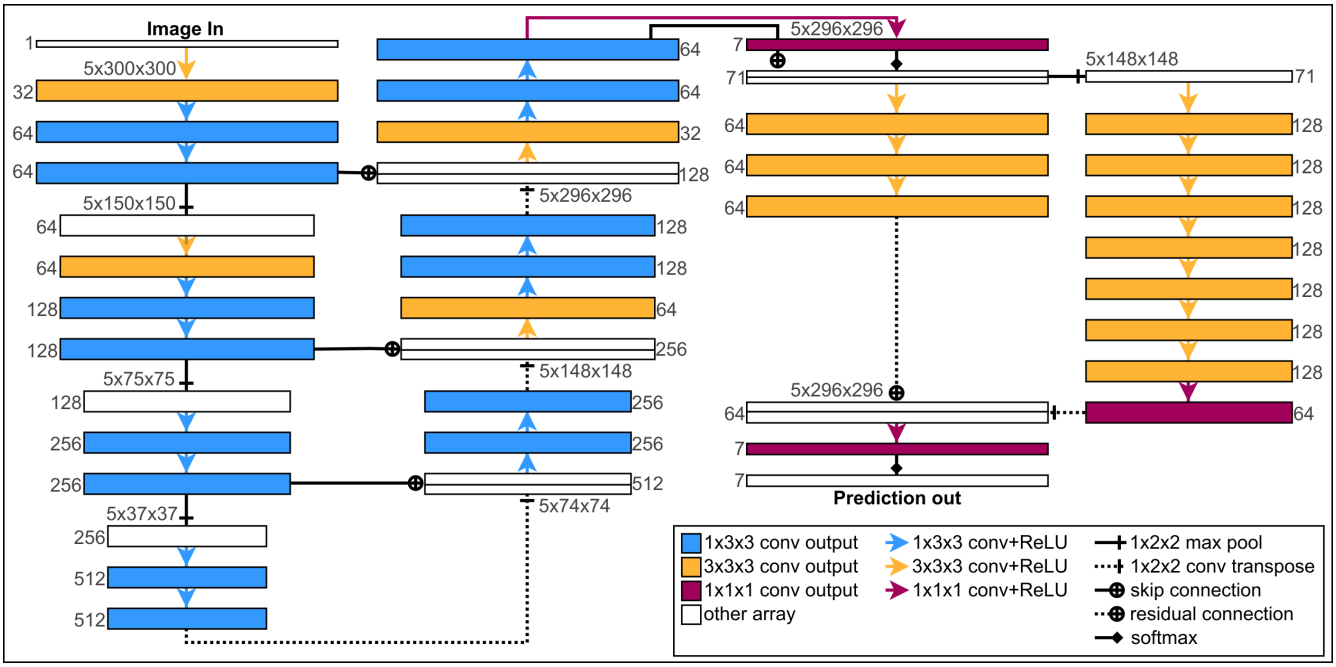

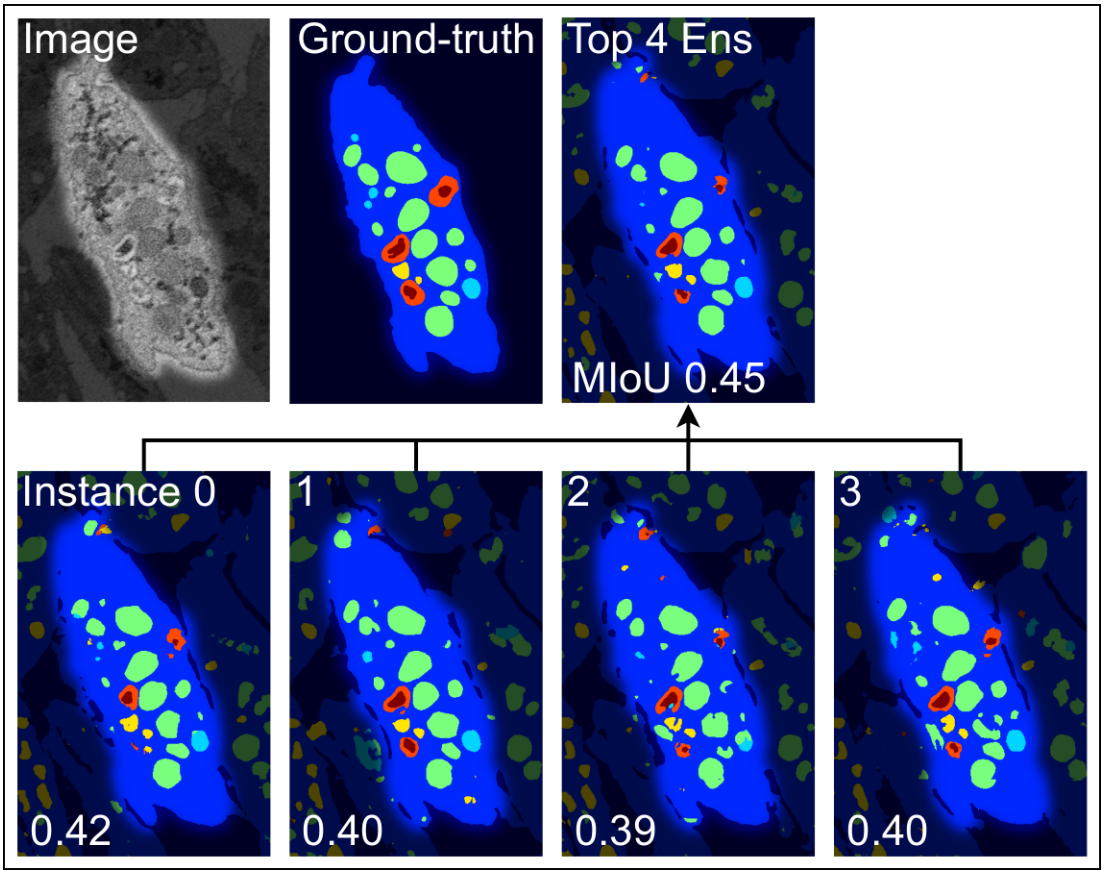

Figure 2. (**Top**) Diagram of the 2D-3D+3x3x3 network architecture. The outputs of a 2D encoder-decoder (left two columns) are connected to a 3D convolutional spatial pyramid (right two columns) to produce a prediction of per-voxel probability distributions across a 3D spatial window. The first two encoder convolution blocks and the last two decoder convolution blocks begin with a 3x3x3 convolution to add additional 3D context into the 2D initial module. (**Bottom**) Illustration of initialization-dependent performance of trained segmentation networks, and exploiting it for ensembling. In the first row, an example image of a cell and its ground-truth segmentation is compared with the result of an ensemble of the top 4 trained 2D-3D+3x3x3 network instances, which has an $\text{MIoU}^{(org)}$ of 0.45. The second row shows the segmentations from the individual instances and their $\text{MIoU}^{(org)}$ scores. The ensemble shows an 8.3% improvement in $\text{MIoU}^{(org)}$ over the best single network alone.

bioRxiv preprint doi: https://doi.org/10.1101/2020.01.05.895003; this version posted February 29, 2020. The copyright holder for this preprint (which was not certified by peer review) is the author/funder. This article is a US Government work. It is not subject to copyright under 17 USC 105 and is also made available for use under a CC0 license.

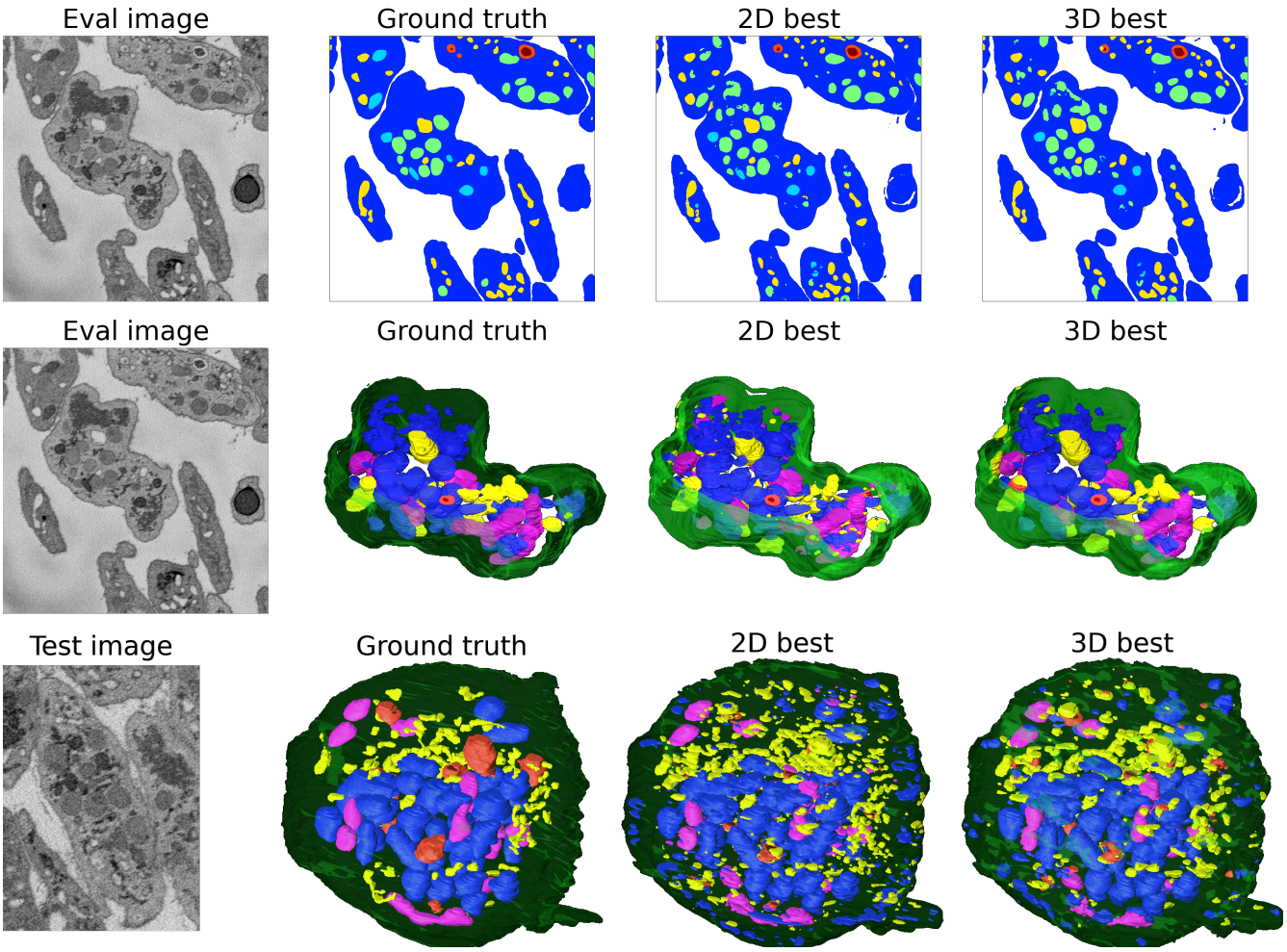

Figure 3. Visualizations of segmentations created by the best 2D and 3D ensembles. (**Top**) Comparison of segmentations on 2D cross-sections of the evaluation data volume, a subset of the Patient 1 platelet sample. Both 2D and 3D ensembles perform similarly on organelle segmentation, making similar mistakes in locations where organelles not within the classification schema are encountered. The 3D ensemble is better at separating cells in regions of near contact between neighbors. (**Middle**) 3D renderings of the center cell within the eval data, taken from the segmentations shown in the top row of this figure. (**Bottom**) Comparison of 3D renderings of segmentations of the test data volume, a cell from the Patient 2 platelet sample. Testing networks on the same biological system from a different physical sample helps gauge how robust they are to image variations due to preparation differences. A comparison of the middle and bottom row of this figure indicates that segmentations of the eval data are better than test data segmentations, an observation supported by Table 1, despite both the eval data and the test data containing cells separate from the ones included in the training data. On one hand, this demonstrates the need for better data preparation or network training procedures to increase robustness to sample variation. On the other hand, the ability of the network to accurately segment new cells within a single sample is valuable for accelerating the segmentation of a large SBF-SEM image volume.

bioRxiv preprint doi: https://doi.org/10.1101/2020.01.05.895003; this version posted February 29, 2020. The copyright holder for this preprint (which was not certified by peer review) is the author/funder. This article is a US Government work. It is not subject to copyright under 17 USC 105 and is also made available for use under a CC0 license.

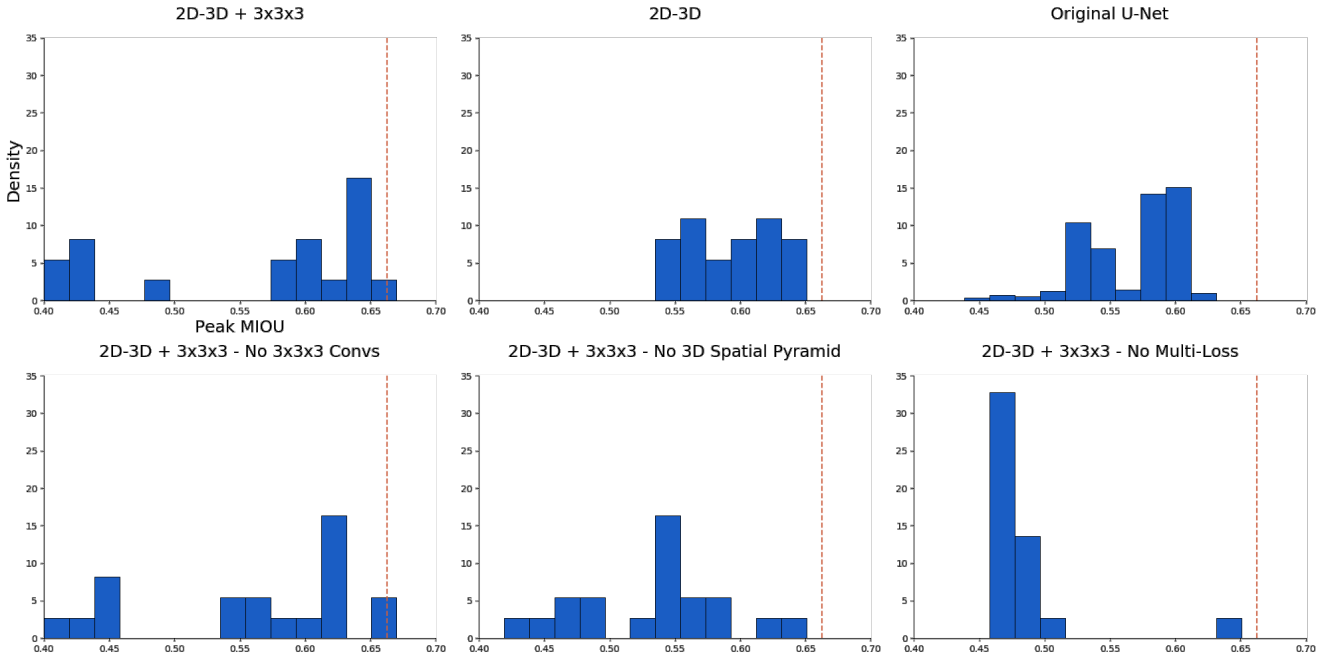

Figure 4. Normalized histograms of peak MIoU on the evaluation data volume for each of the architectures examined in this paper. In order to determine whether one architecture choice is superior to another, the outputs of different trained networks are compared with each other. However, sources of randomness in the training process (initialization of trainable weights from a Xavier uniform distribution, and the random presentation order of training data elements) induce a distribution of final performance metric scores. These scores are random variables, and a single sample per architecture may be insufficient to determine which is better. By empirically approximating the distribution for each architecture, better inferences may be made about architecture design choices. For this figure, multiple instances of the same architecture (26 for 2D-3D nets, 500 for the U-Net) were trained under identical conditions, varying only random number generation seeds. The resulting distributions support the conclusions that 2D-3D networks outperform the 2D U-Net and that multi-loss training is necessary for 2D-3D architectures.

bioRxiv preprint doi: https://doi.org/10.1101/2020.01.05.895003; this version posted February 29, 2020. The copyright holder for this preprint (which was not certified by peer review) is the author/funder. This article is a US Government work. It is not subject to copyright under 17 USC 105 and is also made available for use under a CC0 license.

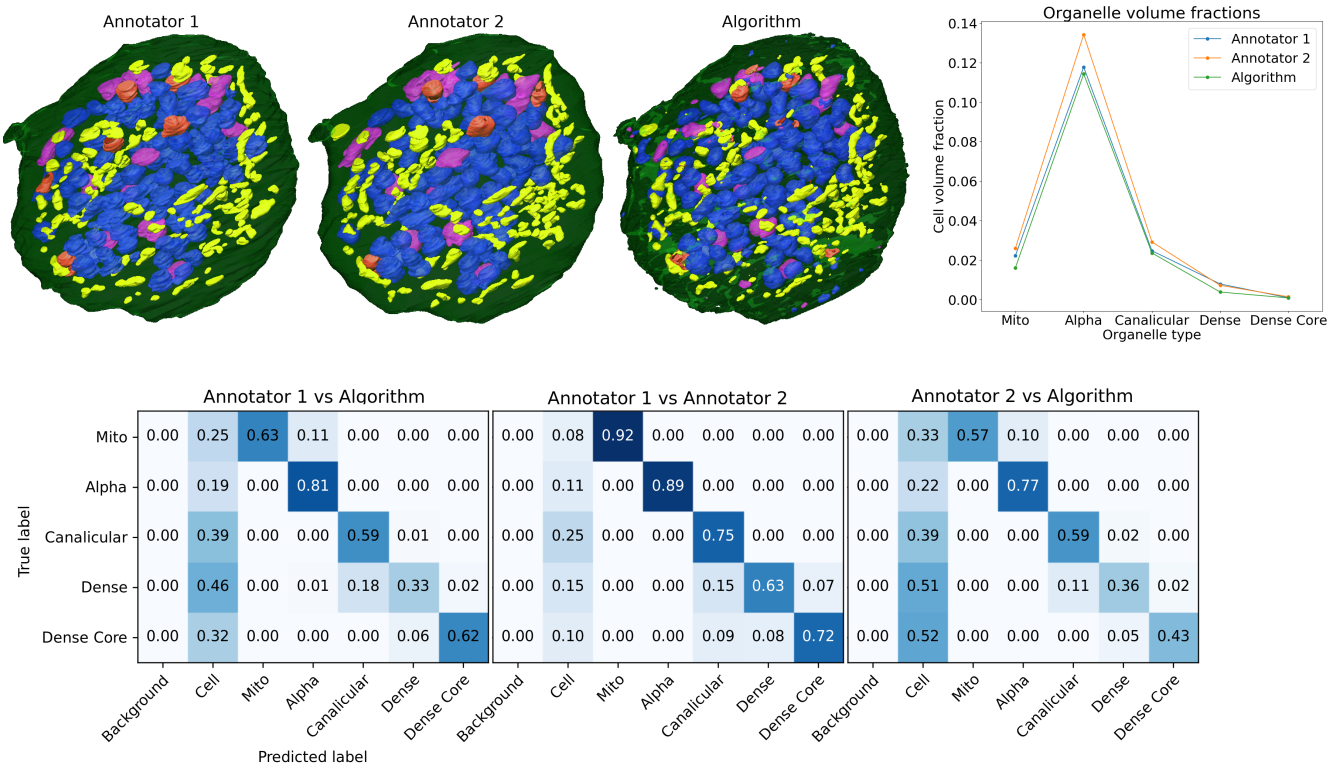

Figure 5. Comparison between two in-lab scientific image annotators and our best algorithm (Top-4 2D-3D+3x3x3) on the annotator comparison dataset, a second cell from the Patient 2 platelet sample. (**Top left**) 3D renderings of segmentations made by the two annotators and our best algorithm. Annotators 1 and 2 do not always agree, but the algorithm detects many small regions which neither annotator labels. (**Top right**) Comparison between the algorithm and annotators at an example downstream biological analysis task - computing the cell volume fraction of each organelle. The cell volume fraction of an organelle is equal to the summed volumes of all organelles in a cell, divided by the cell's volume. To compute this quantity for each organelle, the number of voxels for each organelle label is divided by the number of voxels in the cell. An approximation was necessary for the algorithmic result. Since the algorithm does not distinguish between separate cells in contact with one another, a region for the cell was estimated as all labeled voxels within four voxels of the Annotator 1 cell mask. (**Bottom**) Confusion matrices comparing organelle labelings pairwise between the two annotators and the algorithm. The confusion matrices give a more detailed performance breakdown of the three $\text{MIoU}^{(org)}$ scores obtained for each comparison: 0.571 for Annotator 1 vs. Annotator 2, 0.497 for Annotator 1 vs Algorithm, and 0.483 for Annotator 2 vs Algorithm.

bioRxiv preprint doi: https://doi.org/10.1101/2020.01.05.895003; this version posted February 29, 2020. The copyright holder for this preprint (which was not certified by peer review) is the author/funder. This article is a US Government work. It is not subject to copyright under 17 USC 105 and is also made available for use under a CC0 license.

	Eval MIoU$^{(all)}$	Eval MIoU$^{(org)}$	Test MIoU$^{(org)}$
Top-4 2D-3D+3x3x3	0.686	0.595	**0.446**
Top-5 No 3x3x3 Convs	**0.690**	**0.601**	0.419
Top-3 No Multi-Loss	0.633	0.524	0.338
Top-3 No 3D Pyramid	0.681	0.590	0.421
Top-5 Original U-Net	0.663	0.562	0.371

(a) Ensembles of Networks

2D-3D+3x3x3 (10.3M)	0.665	0.568	0.417
No 3x3x3 Convs (9.9M)	0.667	0.571	0.358
No Multi-Loss (10.3M)	0.652	0.550	0.355
No 3D Pyramid (7.9M)	0.646	0.542	0.376

(b) Single 2D-3D+3x3x3 Network and Ablations

Original U-Net (31.0M)	0.626	0.515	0.334
3D U-Net Thick (2.1M)	0.496	0.348	0.314
3D U-Net Thin (2.0M)	0.613	0.502	0.280
Deeplab + DRN (40.7M)	0.636	0.522	0.130
Deeplab + ResNet101 (59.3M)	0.585	0.456	0.124

(c) Baseline Networks

Table 1. Segmentation algorithm results summary showing mean intersection-over-union (MIoU) across all classes (MIoU$^{(all)}$) on evaluation data and MIoU across organelle classes (MIoU$^{(org)}$) on evaluation and test data. The patient 2 dataset from which the test data is taken contains only a small number of labeled cells among unlabeled ones; we use MIoU$^{(org)}$ to measure test performance since restricting the MIoU stat to labeled regions invalidates `background` and `cell` class statistics. (**a**) Results for the best ensemble from each architecture tested. A top-k ensemble averages the predictions of the best k trained networks as judged by MIoU$^{(all)}$ on the evaluation dataset. (**b**) Results for the best single network from each architecture class. Trainable parameter counts are in parentheses. (**c**) Results from baseline comparison networks. Trainable parameter counts are in parentheses